

# A hierarchical computational model for moving thermal loads and phase changes with applications to Selective Laser Melting

S. Kollmannsberger<sup>a,\*</sup>, A. Özcan<sup>a</sup>, Massimo Carraturo<sup>a,b</sup>, N. Zander<sup>a</sup>, E. Rank<sup>a</sup>

<sup>a</sup>*Chair for Computation in Engineering, Technische Universität München, Arcisstr. 21, 80333 München, Germany*

<sup>b</sup>*Department of Civil Engineering and Architecture, University of Pavia, via Ferrata 3, 27100 Pavia, Italy*

---

## Abstract

Computational heat transfer analysis often involves moving fluxes which induce traveling fronts of phase change coupled to one or more field variables. Examples are the transient simulation of melting, welding or of additive manufacturing processes, where material changes its state and the controlling fields are temperature and structural deformation. One of the challenges for a numerical computation of these processes is their multi-scale nature with a highly localized zone of phase transition which may travel over a large domain of a body. Here, a transient local adaptation of the approximation, with not only a refinement at the phase front, but also a de-refinement in regions, where the front has past is of advantage because the de-refinement can assure a bounded number of degrees of freedom which is independent from the traveling length of the front.

We present a computational model of this process which involves three novelties: a) a very low number of degrees of freedom which yet yields a comparatively high accuracy. The number of degrees of freedom is, additionally, kept practically constant throughout the duration of the simulation. This is achieved by means of the multi-level *hp*-finite element method. Its exponential convergence is verified for the first time against a semi-analytic, three-dimensional transient linear thermal benchmark with a traveling source term which models a laser beam. b) A hierarchical treatment of the state variables. To this end, the state of the material is managed on a separate, octree-like grid. This material grid may refine or coarsen independently of the discretization used for the temperature field. This methodology is verified against an analytic benchmark of a melting bar computed in three dimensions in which phase changes of the material occur on a rapidly advancing front. c) The combination of these technologies to demonstrate its potential for the computational modeling of selective laser melting processes. To this end, the computational methodology is extended by the finite cell method which allows for accurate simulations in an embedded domain setting. This opens the new modeling possibility that neither a scan vectors nor a layer of material needs to conform to the discretization of the finite element mesh but can form only a fraction within the discretization of the field- and state variables.

*Keywords:* additive manufacturing, *hp*-FEM, transient thermal problems, dynamically changing meshes

---

## Contents

<b>1</b>	<b>Introduction</b>	<b>3</b>
<b>2</b>	<b>Thermal analysis with phase changes</b>	<b>4</b>
2.1	Governing equations . . . . .	4
2.2	Discretized weak form . . . . .	5
2.3	Multi-level <i>hp</i> -FEM: Discretization of the primal unknowns . . . . .	6

---

\*Corresponding author

2.4	Examples . . . . .	7
2.4.1	Linear thermal analysis . . . . .	7
2.4.2	Melting bar . . . . .	10
<b>3</b>	<b>Modelling Selective Laser Melting</b>	<b>13</b>
3.1	Finite Cell Method . . . . .	13
3.2	Multi-level <i>hp</i> method and the finite cell method at work . . . . .	15
<b>4</b>	<b>Conclusions</b>	<b>17</b>

## 1. Introduction

The computational analysis of powder bed fusion processes such as e.g. selective laser melting (SLM) is challenging due to many reasons. The most prominent include:

1. highly localized and moving strong temperature gradients
2. non-linearities due to temperature dependent coefficients and phase changes of the material
3. growing and possibly geometrically complex computational domains
4. large range of scales in both space and time
5. coupled multi-physics

This article presents a methodology for the computational modeling of the temperature evolution in a powder bed fusion process taking into account the first three issues. While we incorporate the non-linearities due to temperature dependent coefficients and phase changes of the material using the rather standard latent heat model first presented in [1], special focus lies on the discretization of the highly localized and moving strong temperature gradients and on the representation of growing computational domains.

The evolution of temperature fields in space is a diffusion dominated process which can be well resolved by the finite element method. Many commercial packages are available, of which ABAQUS® and ANSYS® are two popular choices for applied research. These and other commercial packages provide a wealth of physical models, but their discretizational technology is mostly limited to linear, at most quadratic finite elements. Therefore, the resolution of local gradients is limited to  $h$ -refinements, i.e. refining the mesh size towards singularities.

Strong gradients, however, can most efficiently be resolved by  $hp$ -finite elements which vary the size of the element  $h$  locally as well as the polynomial degree of the trial/test space  $p$  [2, 3]. While  $hp$ -fem leads to efficient discretizations where error estimators are used to drive an adaptive scheme, it also provides excellent accuracy in cases where the solution characteristic is known a priori. This is the case for the simulation of powder bed fusion processes because the area of refinement is well defined by the location of the laser spot where sudden, high temperatures cause phase changes in the material.

Moreover, most simulations of powder bed fusion processes use static discretization schemes, i.e. the mesh is refined towards the entire laser path and kept fixed at all time-steps. As a consequence, the necessary number of degrees of freedom is directly proportional to the length of the laser path. However, high gradients are local to the laser spot itself and not distributed along all of its path. Therefore, the number of degrees of freedom should be independent of the length of the laser path and at best constant over time. To this end, transient refinement and de-refinements of the discretization throughout the run time of the simulation is necessary to keep the refinement local to the current position of the laser. Only recently, discretizations have appeared that utilize these kind of transient meshes for computational SLM analysis, see e.g. [4, 5, 6] and references therein. To the authors' knowledge, all of these contributions exploit  $h$ -refinements for low order polynomials, only. Transient  $h$ -refinements for higher order polynomials have not been used in that context although even transient  $hp$  codes do exist along with instructive literature, see e.g. [7, 8, 9, 10] and the introduction of [11] for a recent overview.

Another important aspect is the treatment of the state variables. While the evolution of temperature is a diffusive process, the evolution of the material state is not. Solidified material does not diffuse into regions containing powder. Additionally, material interfaces may not coincide with the boundaries of the finite elements. For example, material may need to be added in form of powder in a way which does not necessarily conform to the finite element discretization. In the paper at hand, we propose to provide this flexibility by discretizing the material coefficients independently of the underlying discretization of the field variables.

The article is structured as follows: We start by introducing the governing equations in section 2.1 and present its discretized weak form in section 2.2. We then give a quick introduction into the recently introduced multi-level  $hp$ -finite element method [11], which provides  $hp$ -discretizations on transient meshes. To evaluate its accuracy, we first present results for a transient but linear, three-dimensional benchmark resembling a SLM process in section 2.4.1 before proceeding to evaluate the scheme against a transient non-linear benchmark involving phase changes and latent heat in section 2.4.2.

We then proceed to combine the multi-level  $hp$ -method with the finite cell method in section 3.1 which was initially designed to avoid boundary conforming mesh generation for complex domains. We use this concept to treat state and field variables on different discretizations. Section 3.2 then presents an example computing the evolving interface of a structure. Herein, two independent and transiently changing discretizations are used for state and field variables. Their separate treatment combined with the multi-level  $hp$  method allows for a relatively low number of degrees of freedom which stay almost constant throughout the simulation process.

## 2. Thermal analysis with phase changes

This section sets out to describe a new discretizational scheme for thermal analysis with phase changes. To clear the view, we neglect effects of radiation and mass transfer even though they have physical relevance in practical examples.

### 2.1. Governing equations

In this spirit, let us consider a domain,  $\Omega \subset \mathbb{R}^n$  with boundary  $\partial\Omega$ , where  $n$  is the number of space dimensions. The governing nonlinear transient heat conduction equation with phase-change, written in terms of volumetric enthalpy  $H = H(T)$  and temperature  $T = T(\mathbf{x})$  fields, has been investigated by many researchers. In the sequel, we closely follow the presentation given in [12] which reads:

$$\frac{\partial H}{\partial t} - \nabla \cdot (k \nabla T) = Q \quad \text{in } \Omega, \quad (1)$$

where  $t$  is the time,  $k$  is the thermal conductivity and  $Q$  is the heat source. Equation (1) is subjected to the initial condition

$$T(\mathbf{x}, t = 0) = T_0(\mathbf{x}) \quad \text{in } \Omega. \quad (2)$$

Dirichlet, Neumann, convection and radiation boundary conditions can be defined on non-overlapping boundaries:

$$T = T_w(\mathbf{x}) \quad \text{on } \partial\Omega_T, \quad (3)$$

$$(k \nabla T) \cdot \mathbf{n} = q(\mathbf{x}) \quad \text{on } \partial\Omega_q, \quad (4)$$

$$(k \nabla T) \cdot \mathbf{n} = h_{conv}(T_\infty - T(\mathbf{x})) \quad \text{on } \partial\Omega_c, \quad (5)$$

$$(k \nabla T) \cdot \mathbf{n} = \sigma \epsilon (T^4 - T_\infty^4) \quad \text{on } \partial\Omega_r, \quad (6)$$

where  $T_w$ ,  $q$ ,  $h_{conv}$  and  $T_\infty$  are the prescribed temperature, prescribed heat flux, thermal convection coefficient and ambient temperature, respectively. Further,  $\sigma$  is the Stefan-Boltzmann constant and  $\epsilon$  represents the emissivity.

The volumetric enthalpy function is defined as

$$H(T) = \int_{T_{\text{ref}}}^T \rho c(T) dT + \rho L \tilde{f}_{pc}(T), \quad (7)$$

where  $\rho, c, L, T_{\text{ref}}$  and  $f_{pc}$  denote density, specific heat capacity, latent heat, a reference temperature and a phase-change function, respectively. The function  $f_{pc}$  depends on the nature of the process. In an isothermal phase change, the temperature  $T_m$  stays constant during the phase change and is defined by a heavyside step function:

$$\tilde{f}_{pc}(T) = \begin{cases} 0 & T \leq T_m \\ 1 & T > T_m \end{cases}, \quad (8)$$

see fig. 1a for an illustration. For numerical reasons, the function  $\tilde{f}_{pc}$  is regularized by a smooth function as

$$f_{pc}(T) = \frac{1}{2} \left[ \tanh \left( S \frac{2}{T_l - T_s} \left( T - \frac{T_s + T_l}{2} \right) \right) + 1 \right], \quad (9)$$

which is depicted in fig. 1b for different values of  $S$  which controls the smoothing.

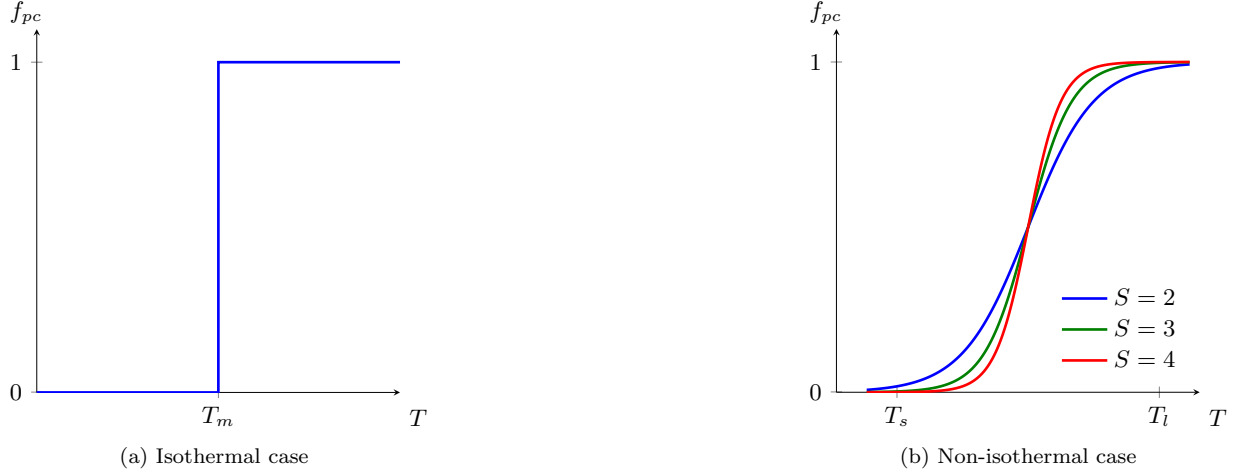


Figure 1: Phase change function  $f_{pc}$

A substitution of eq. (7) in eq. (1) leads to the temperature based phase-change model:

$$\rho c \frac{\partial T}{\partial t} + \rho L \frac{\partial f_{pc}}{\partial t} - \nabla \cdot (k \nabla T) = Q \quad \text{in } \Omega. \quad (10)$$

Equation (10) reduces to the classical transient heat conduction equation, when the latent heat term is neglected.

## 2.2. Discretized weak form

The governing partial differential eq. (10) subjected to the initial condition given by eq. (2) and the Dirichlet, Neumann and convection boundary conditions given in eqs. (3) to (5), respectively is now discretized in time and space. For the spatial discretization, the Bubnov-Galerkin finite element method is ideally suited due to the mainly diffusive nature of the described process. To this end, the set  $\mathcal{V}$  of admissible solutions  $T$  and a set  $\mathcal{V}_0$  of admissible test functions  $\psi$  is defined as

$$\mathcal{V} = \{v \in H^1(\Omega), \quad v = T_w(\mathbf{x}, t) \text{ on } \partial\Omega_T\} \quad \text{and} \quad \mathcal{V}_0 = \{v \in H^1(\Omega), \quad v = 0 \text{ on } \partial\Omega_T\}, \quad (11)$$

where  $H^1$  is the Hilbert space. The weak form of eqs. (2) to (5) then reads:

Find  $T \in \mathcal{V}$ , such that

$$\int_{\Omega} \psi \rho c \frac{\partial T}{\partial t} d\Omega + \int_{\Omega} \psi \rho L \frac{\partial f_{pc}}{\partial t} d\Omega + \int_{\Omega} \nabla \psi \cdot (k \nabla T) d\Omega = \int_{\Omega} \psi Q d\Omega + \int_{\partial\Omega_n} \psi q d\Gamma + \int_{\partial\Omega_c} \psi h(T_{\infty} - T) d\Gamma. \quad (12)$$

In the framework of the Bubnov-Galerkin finite element method, solution field and test functions are approximated by the same shape functions  $N_i$  as follows:

$$T(\mathbf{x}, t) \approx T_h(\mathbf{x}, t) = \sum_{i=1}^n N_i(\mathbf{x}) T_i(t), \quad \psi(\mathbf{x}, t) \approx \psi_h(\mathbf{x}, t) = \sum_{i=1}^n N_i(\mathbf{x}) \psi_i(t), \quad (13)$$

where  $T_i$  and  $\psi_i$  are the unknown coefficients. Substituting the approximations eq. (13) into the weak form eq. (12) yields the following semi-discrete equilibrium equation:

$$\begin{aligned}
\mathbf{C}\dot{\mathbf{T}} + \dot{\mathbf{L}} + \mathbf{K}\mathbf{T} &= \mathbf{F} \\
C_{ij} &= \int_{\Omega} \rho c N_i N_j \, d\Omega \\
\dot{L}_i &= \int_{\Omega} \rho L N_i \frac{\partial f_{pc}}{\partial t} \, d\Omega \\
K_{ij} &= \int_{\Omega} \nabla N_i \cdot (k \nabla N_j) \, d\Omega + \int_{\partial\Omega_c} h N_i N_j \, d\Gamma \\
F_i &= \int_{\Omega} N_i Q \, d\Omega + \int_{\partial\Omega_q} N_i q \, d\Gamma + \int_{\partial\Omega_c} h N_i T_{\infty} \, d\Gamma
\end{aligned} \tag{14}$$

where  $\mathbf{C}$  is the capacitance matrix,  $\mathbf{K}$  is the conductivity matrix,  $\mathbf{L}$  is the latent heat vector,  $\mathbf{F}$  is the load vector and  $\mathbf{T}$  is the temperature coefficient vector. The residual vector  $\mathbf{R}$  for the transient nonlinear analysis is obtained by using the backward Euler time integration scheme for the terms  $\dot{\mathbf{L}}$  and  $\dot{\mathbf{T}}$  in eq. (14):

$$\mathbf{R}_{n+1} = \mathbf{F}_{n+1} - \mathbf{C}_{n+1} \frac{\mathbf{T}_{n+1} - \mathbf{T}_n}{\Delta t} - \frac{\mathbf{L}_{n+1} - \mathbf{L}_n}{\Delta t} - \mathbf{K}_{n+1} \mathbf{T}_{n+1} \stackrel{!}{=} \mathbf{0}. \tag{15}$$

The subscripts  $n$  and  $n+1$  represent evaluations at time  $t$  and  $t + \Delta t$ , respectively. In order to solve this nonlinear equation, we use an iterative incremental scheme, where the current temperature vector is:

$$\mathbf{T}_{n+1}^{i+1} = \mathbf{T}_{n+1}^i + \Delta \mathbf{T}^i. \tag{16}$$

$$\mathbf{J}_{n+1}^i \Delta \mathbf{T}^i = \mathbf{R}_{n+1}^i. \tag{17}$$

Equation (17) shows the incremental system to be solved, where  $\mathbf{J}$  is the tangent Jacobian matrix which is defined as

$$\mathbf{J}_{n+1}^i = - \left. \frac{\partial \mathbf{R}}{\partial \mathbf{T}} \right|_{n+1}^i = \mathbf{K}_{n+1}^i + \frac{\mathbf{C}_{n+1}^i}{\Delta t} + \frac{\mathbf{L}'^i|_{n+1}}{\Delta t}. \tag{18}$$

The latent heat contribution  $\mathbf{L}'$  of the Jacobian matrix  $\mathbf{J}$  is:

$$L'_{ij} = \int_{\Omega} \rho L \frac{\partial f_{pc}}{\partial T} N_i N_j \, d\Omega, \tag{19}$$

where we approximate the temperature derivative of the function  $f_{pc}$  as suggested in [12]:

$$\left. \frac{\partial f_{pc}}{\partial T} \right|_{n+1}^i = \frac{f_{pc}(T_{n+1}^i) - f_{pc}(T_n)}{T_{n+1}^i - T_n}, \tag{20}$$

### 2.3. Multi-level hp-FEM: Discretization of the primal unknowns

It lies in the nature of the SLM process to induce phase change locally by application of a highly focused laser beam. This heat flux is discretized in  $\mathbf{F}$  and it induces high temperatures locally which diffuse rapidly into the domain. The resulting high but non-singular gradients are best captured by *hp* finite element schemes.

Implementations of *hp*-finite elements are widely available in the scientific community, see e.g. [3, 13, 14, 15, 16]. Research in the field of isogeometric analysis has further amplified the available code-basis, see

e.g. [17]. However, the situation is less comfortable in cases where dynamic *hp*-discretizations are necessary in three dimensions. This is due to the fact that handling degrees of freedom on changing mesh topologies proves to be difficult in 3D. The recently introduced multi-level *hp*-method aims at alleviating this burden. An *en-detail* description of the method is given in [18, 11, 19] along with a review of other, related methods.

Classic *hp*-approaches replace finite elements with refined elements and constrain hanging nodes, edges and faces to re-establish a  $C^0$ -compatible, global trial and test space. The multi-level *hp*-method takes a completely different approach. Its underlying idea is to retain coarse elements in the mesh. The refinement is then constructed hierarchically such that global  $C^0$ -continuity and linear independence is maintained by construction. This renders post-constraining unnecessary. The principle idea is depicted in fig. 2a) in one dimension. Compatibility is ensured by applying homogeneous boundary conditions on all boundaries of the overlay mesh. In one dimension this translates to deactivating all nodal degrees of freedom on the overlay meshes which correspond to the boundary of the overlay. Linear independence is guaranteed by deactivating the high-order modes on the lower levels. Thereby, high-order shape functions are *h*-refined as well and finite element spaces are constructed which are very close those generated by classical *hp*-finite element methods [20]. The simple rule set of activating and de-activating nodal and edge modes directly translates to two- and three-dimensions as depicted in fig. 2b) and c) if face and internal modes are accounted for likewise.

#### 2.4. Examples

This section addresses the first two computational challenges stated in the introductory section 1. To this end we evaluate the accuracy of the multi-level *hp*-method by means of a comparison to two semi-analytical benchmarks, which resemble SLM-typical problems: a moving laser source in linear thermodynamics in section 2.4.1 and a variant of Stefan's problem involving phase changes in section 2.4.2.

##### 2.4.1. Linear thermal analysis

It was already demonstrated in [11] that strong gradients in a stress field can be captured accurately on moving discretizations. The paper at hand investigates the (parabolic) heat equation commonly used for modelling SLM processes. We consider the following simplified form of eq. (21)

$$\rho c \frac{\partial T}{\partial t} - \nabla \cdot (k \nabla T) = q \quad \text{in } \Omega. \quad (21)$$

where  $q$  is the Gaussian surface distributed heat source:.

$$\begin{aligned} q(x, z, t) &= \lim_{b \rightarrow 0} \frac{6\sqrt{3}Q}{\pi\sqrt{\pi}ab} \int_0^{\inf} \exp\left(-3\frac{y^2}{b^2}\right) dy \times \frac{1}{c} \exp\left[-3\frac{x^2}{a^2} - 3\frac{(z-vt)^2}{c^2}\right] \\ &= \frac{3Q}{\pi a} \times \frac{1}{c} \exp\left[-3\frac{x^2}{a^2} - 3\frac{(z-vt)^2}{c^2}\right], \end{aligned} \quad (22)$$

which is also commonly referred to as an elliptical disk heat source, see e.g [21]. Its distribution parameters  $a$  and  $c$  are referred to as its radii and the maximum heat power is denoted by  $Q$ . The center of the heat source travels with a constant speed  $v$  along the path  $A-B$  on the upper boundary of the semi-infinite body given in fig. 3a. It is depicted in fig. 3b along with its local coordinate system.

The analytical solution of this transient temperature field was first introduced by [21]. Herein, the space and time dependent temperature  $T(x, z, t)$  is given as the initial temperature  $T_0$  plus a time integral from the start of the process at  $t = 0$  to the time of interest  $t$ :

$$T(x, z, t) = T_0 + \frac{3\sqrt{3}}{\pi\sqrt{\pi}} Q / (\rho h c) \times \int_0^t \frac{\exp\left[-3\frac{x^2}{12\kappa(t-t') + a^2}\right]}{\sqrt{12\kappa(t-t') + a^2} \sqrt{12\kappa(t-t')}} \times 2A dt', \quad (23)$$

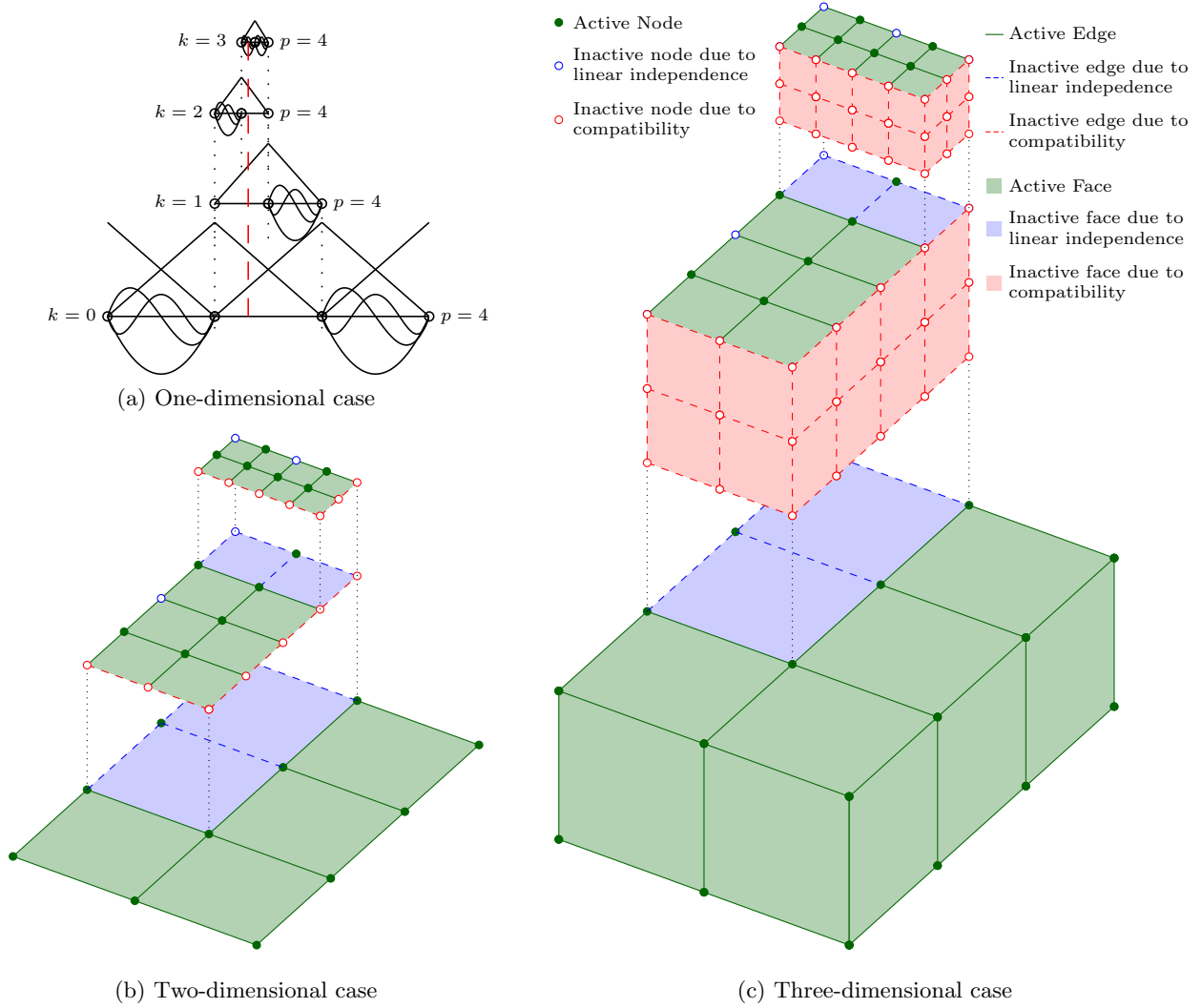


Figure 2: Conceptual idea of the multi-level  $hp$ -method following [18, 11, 19]

whereby the abbreviation  $A$

$$A = A(z, t, t') = \frac{\exp \left[ -3 \frac{(z - vt')^2}{12\kappa(t - t') + c^2} \right]}{\sqrt{12\kappa(t - t') + c^2}}, \quad (24)$$

and  $\kappa = k/(\rho h_c)$  is the thermal diffusivity. The parameters of the setup are chosen in the range of a typical SLM scanning process and listed in table 1.

Radiation-convection boundary conditions are imposed on the bottom and side surfaces by setting the environmental temperature to  $T_{env} = 0^\circ\text{C}$  and the convection coefficient to  $h_{conv} = 0.0 \text{ [W/m}^2\text{°C]}$ . This leads to an approximation of the temperature at the surfaces cutting the considered block out of the half-domain which would otherwise be given by eq. (23). However, these cut-off surfaces are far enough away for this approximation to have any notable effect on the temperature distribution along the path  $A-B$ . The time domain was discretized by 500 hundred time steps with  $\Delta t = 4 \text{ [\mu sec]}$ .

The base mesh of the multi-level  $hp$ -discretization is depicted in fig. 3a and consists of  $2 \times 2 \times 2$  elements. This base mesh is refined by successively superposing finer overlay elements that halve the size of their



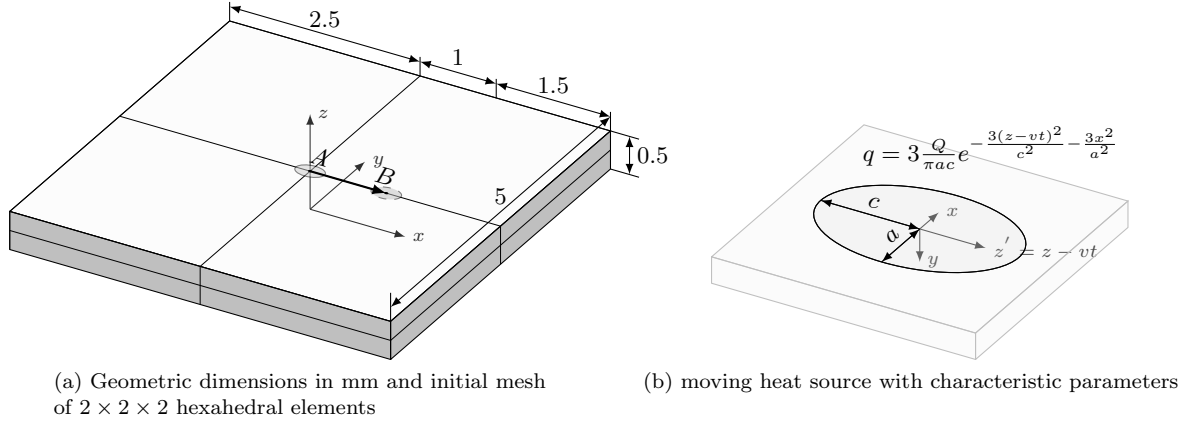


Figure 3: Problem Setup

Specific heat ( $h_c$ )	600 J/(kg°C)	Heat Power (Q)	50.83 W
Density ( $\rho$ )	7820 kg/m <sup>3</sup>	Laser speed ( $v$ )	0.5 m/s
Heat Conductivity ( $k$ )	29 W/(m°C)	Half radius a	0.1 mm
		Half radius c	0.15 mm

Table 1: Material and load parameters for the benchmark defined in fig. 3

parent. Figure 4 gives an impression of the resulting mesh for five overlays. A possible measure of resolution is to relate the numbers of elements per twice the smallest distribution parameter of  $q$  defined in eq. (22), here  $a = 0.1[\text{mm}]$ . For the base mesh, this ratio is  $0.2[\text{mm}]/2.5[\text{mm}] = 0.08$  which is then doubled by each level of refinement i.e. levels one to five lead to: 0.16, 0.32, 0.64, 1.28, 2.56 elements per  $2a$ . The refinement is not carried out uniformly but towards a bounding box which defines the zone of maximum  $h$  refinements. It is initially located at the center of the laser beam, has the initial dimensions  $0.125[\text{mm}]/0.0625[\text{mm}]/0.03[\text{mm}]$ , and is oriented along the global  $x/y/z$ -axis. During the scanning process, the rear face of the bounding box is kept fixed until it has an elongation of  $0.7[\text{mm}]$ . The size of the bounding box then stays fixed and the bounding box follows the laser path with constant dimensions until its end.

The results for the temperature are depicted for different time-steps in fig. 5. While the colors in the picture correspond to the refinement depth, the discretization is warped in the global  $z$ -direction using the computed temperature field. The picture series demonstrates the dynamic change of the discretization over time, which allows the refinement zone to stay local to the moving laser spot.

Figure 6a depicts the spatial solution of the temperature along the laser path, i.e. the cutline between point  $A$  and  $B$  in fig. 3 for different polynomial degrees. Figure 6b records the temperature history of a material point located at the coordinates  $x=0.25, y=0.0, z=0.1$ . It can clearly be seen how increasing the polynomial degree  $p$  of the approximation helps in increasing the solution accuracy.

To obtain a better insight into the convergence behavior,  $p$ -extensions (i.e. sequence of computations with increasing polynomial degrees) were carried out on different  $h$ -refinements. To this end, the analytical solution given by eq. (23) was computed using the function `integral` in `matlab`<sup>®</sup>. This function performs an adaptive quadrature with a relative tolerance of  $1e-6$  [22]. The computation was carried out at 1000 equidistant points along the laser path between point  $A$  and  $B$ <sup>1</sup>. and its deviation from the numerical approximation obtained by the multi-level  $hp$ -method served as an error measure in the sense of a discrete- $L_2$  norm:

$$\|e\|_{L_2} = \sqrt{\frac{\sum_{i=0}^{1000} (T_{san,i} - T_i)^2}{\sum_{j=0}^{1000} T_{san,j}^2}} \times 100. \quad (25)$$

<sup>1</sup>in fig. 3a

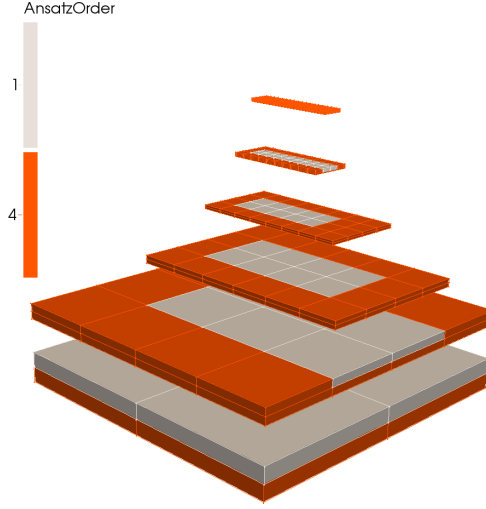


Figure 4: Local 3D multi-level  $hp$  mesh

Herein  $T_{san}$  represents the semi-analytical solution of eq. (23), and  $T_i$  is the temperature obtained by the multi-level  $hp$ -method at the  $i_{th}$  point.

The convergence plots are presented in two forms for the same data. Figure 7a gives the number of degrees of freedom versus the discrete, relative  $L_2$  error computed by eq. (25) whereby both axis possess logarithmic scale. Figure 7b displays the same data, but the abscissa is scaled by the third root of the degrees of freedom. The blue line with the filled dots labeled ‘uniform  $h$ ,  $p=1$ ’ represents the accuracy obtained by discretizing the domain uniformly starting with a mesh of size  $2 \times 2 \times 2$ , then  $4 \times 4 \times 4$ , then  $8 \times 8 \times 8$  up to  $32 \times 32 \times 32$  elements. The relative error does not fall below 27% at 35,937 degrees of freedom for this strategy. This demonstrates how poorly a uniform refinement converges. All other curves are obtained by performing a multi-level  $hp$ -refinement towards the bounding box as described above. Consider the blue line with the blue circles labeled “1 ml,  $p=1...10$ ”. The mesh here consists of the base mesh plus one refinement. For each dot, the mesh stays fixed and the polynomial degree is increased from one to ten along the line. The error now drops to 6% for  $p = 10$ , and its decrease is exponential. This is indicated by the straight line in fig. 7b. It is noteworthy that each added level of  $h$ -refinement upon which a  $p$ -extension is carried out uniformly leads to better results with less degrees of freedom only until level four. Level five is worse again. Here, too many degrees of freedom are spent in parts of the domain where the error is already low. This may be avoided by use of an error estimator. In any case, a very good discretization is obtained using four refinements with a polynomial degree of four. Here, only 3857 degrees of freedom are needed to obtain an error of 1.3%. At this point, the results delivered by the multi-level  $hp$ -strategy are approximately twenty times more accurate at ten times less the degrees of freedom than a bold  $h$ -refined strategy for this setup.

#### 2.4.2. Melting bar

In this section, we evaluate the numerical approximation to the isothermal phase change model that is introduced in section 2. We are especially interested in the methods ability to accurately resolve the interface between liquid and solid parts of the domain. Unfortunately, exact solutions to eq. (10) are only available for very few idealized situations in a dimensionally reduced setting.

We consider the two-phase problem of a one-dimensional semi-infinite bar. The bar is initially solid with a constant temperature  $T_s$ . The boundary condition at  $x = 0$  is then suddenly changed to a stationary temperature  $T_l$  which is larger than the melting temperature  $T_m$ . The analytical solution was originally described in [23] and is known in the literature as *Neumanns’s method*, see e.g. [24, 25].

The sudden change of the temperature from  $T_s$  to  $T_l$  causes the bar to melt. The position of the interface

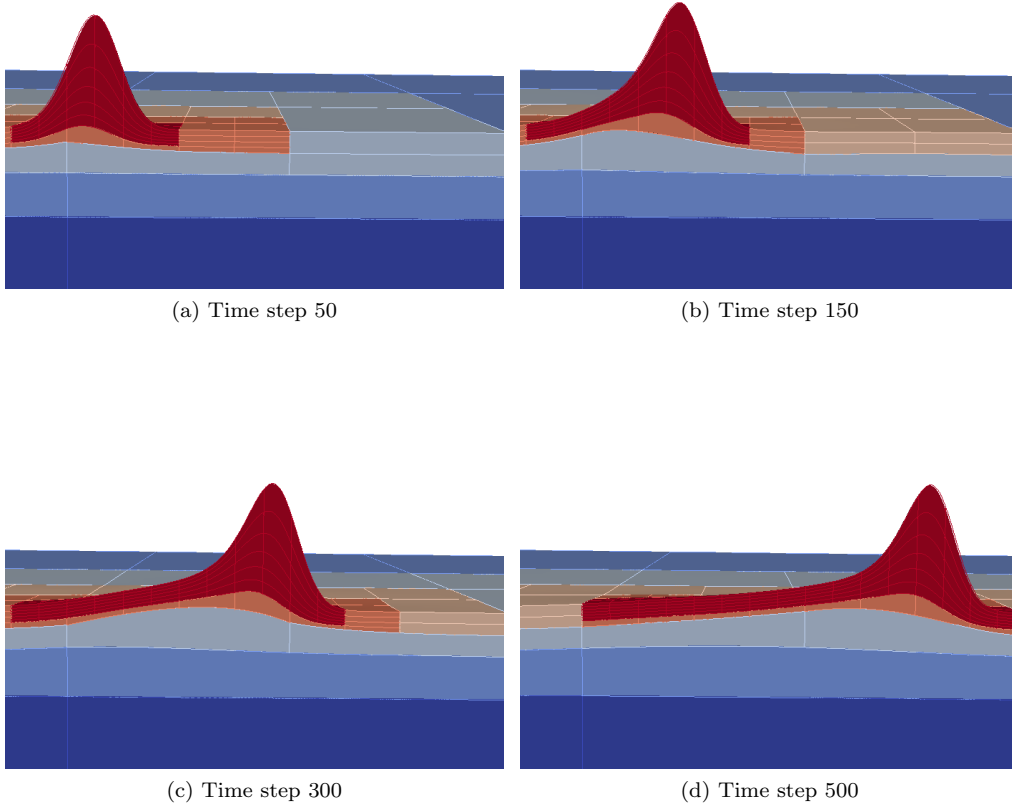


Figure 5: Temperature solution at different time steps and adapted refinements depth

between melt and solid is given by:

$$X(t) = 2\lambda\sqrt{\alpha_l t}, \quad (26)$$

where  $t$  is the time and  $\alpha_l$  is the diffusivity of the material in its liquid state. The constant  $\lambda$  in equation 26 is computed by solving the following non-linear equation

$$\frac{St_l}{\exp(\lambda^2)\text{erf}(\lambda)} - \frac{St_s\sqrt{\alpha_s}}{\sqrt{\alpha_l}\exp(\alpha_l\lambda^2/\alpha_s)\text{erfc}(\lambda\sqrt{\alpha_l/\alpha_s})} = \lambda\sqrt{\pi}, \quad (27)$$

where  $St_l$  and  $St_s$  are the Stefan number of liquid and solid phases respectively. They can be computed as follows:

$$St_l = \frac{C_l(T_l - T_m)}{L}, \quad St_s = \frac{C_s(T_m - T_s)}{L}. \quad (28)$$

In eq. (28),  $L$  is the latent heat of fusion, and  $C_l$  and  $C_s$  are the heat capacity of the liquid and solid phases,

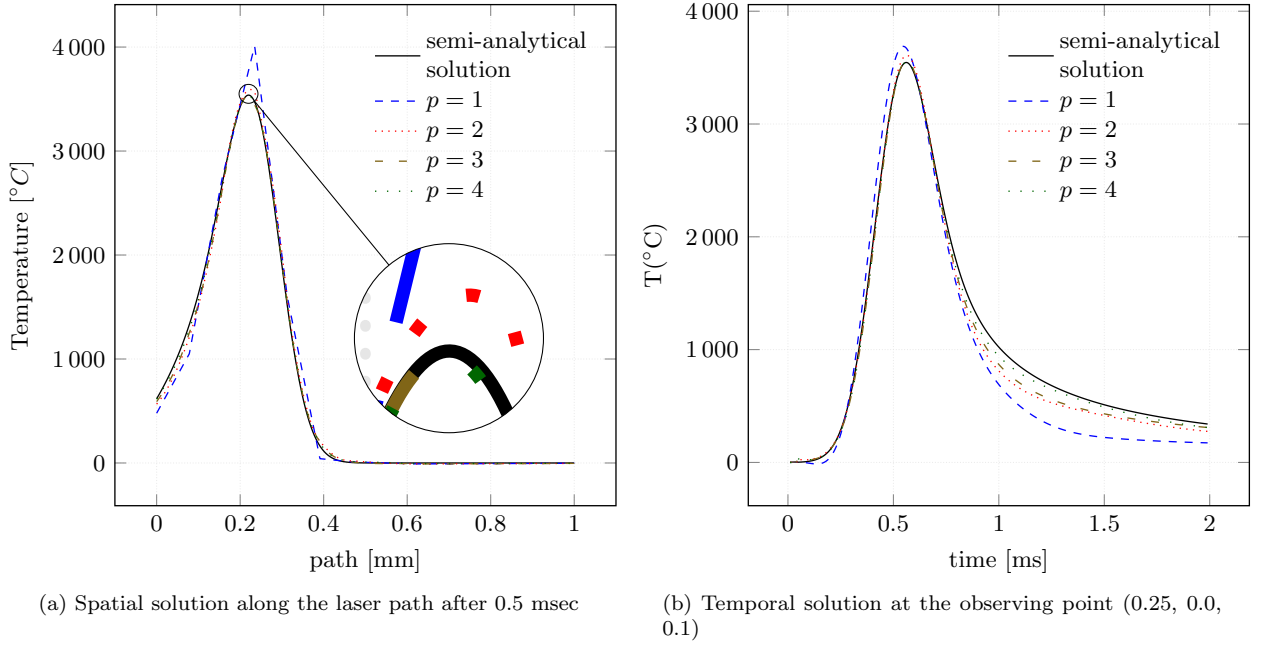


Figure 6: Temperature solution for 4 multi-level refinements for polynomial orders  $p = 1 \dots 4$ .

respectively. The analytical temperature distribution over the semi-infinite slab is given by

$$T(\mathbf{x}, t) = \begin{cases} T_l - (T_l - T_m) \frac{\text{erf}(x/2\sqrt{\alpha_l t})}{\text{erf}(\lambda)} & \text{if } x \leq X(t) \\ T_s + (T_m - T_s) \frac{\text{erfc}(x/2\sqrt{\alpha_s t})}{\text{erfc}(\lambda\sqrt{\alpha_l/\alpha_s})} & \text{if } x > X(t) \end{cases}. \quad (29)$$

Figure 8 illustrates the dimensions of the bar which is used for validation of the numerical scheme. The bar consists of pure Titanium and is assumed to have the thermo-physical properties provided in table 2. These lead to the constant  $\lambda = 0.388150542167233$ , which is computed from eq. (27). On the face at  $x = 0.1$  the analytical solution is imposed as a constant Dirichlet boundary condition to emulate the semi-infinite domain. The simulation was carried out on a base mesh with 10 finite elements of order  $p = 3$  with four multi-level  $hp$ -refinements. The time domain was discretized by a backward Euler scheme with a time step of  $dt = 1[\text{s}]$ .

Figure 9a shows the corresponding numerical solution of the temperature along the  $x$ -direction of the bar at different time steps together with the analytical solution. The kink in the solution at the melting temperature  $T_m$  is clearly visible. It stems from the latent heat contribution represented by  $\dot{L}_i$  in the semi-discrete weak form given in eq. (14). The lens zoom depicts how close the numerical solution resembles its analytic counterpart. Figure 9b depicts the evolution of the temperature at the point  $x = 0.01[\text{m}]$  which is very close to the Dirichlet interface and therefore difficult to catch. The kink at  $T_m$  is also clearly visible and well captured by the numerical scheme.

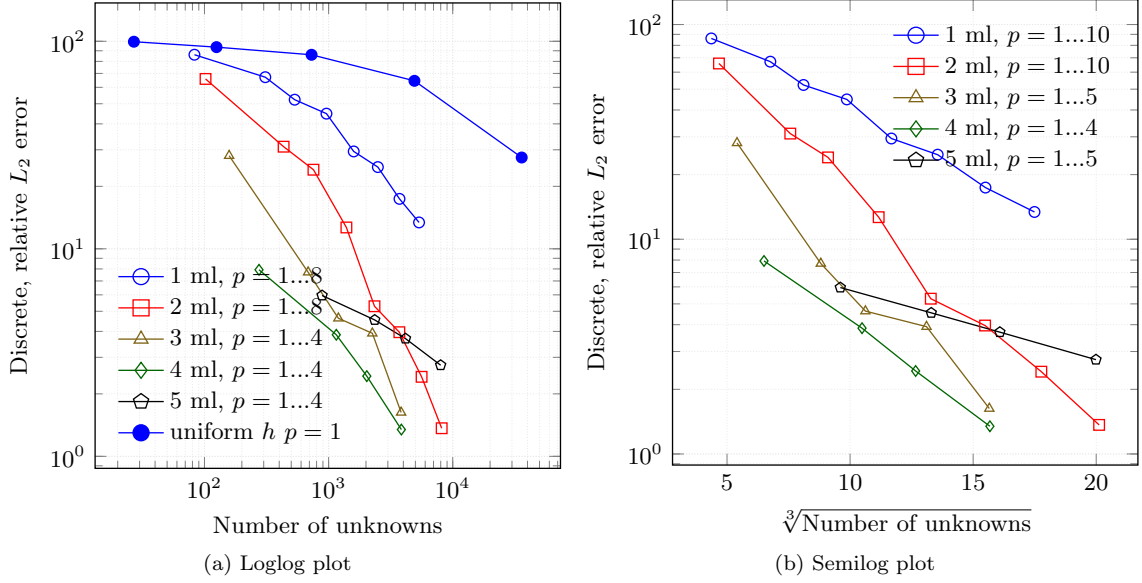


Figure 7: Convergence in discrete  $L_2$ -norm starting from a  $2 \times 2 \times 2$  base mesh and hierarchically refining in  $h$  2, 3 or 4 times (used abbreviations: ml = multi-level  $hp$  refinement)

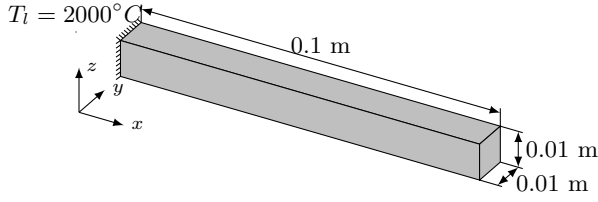


Figure 8: Problem setup of the melting bar

$T_m$	1670 °C
$T_l$	2000 °C
$T_s$	1500 °C
$\rho$	$4.51 \times 10^3 \text{ kg/m}^3$
$c_l = c_s$	520 J/(m <sup>3</sup> °C)
$k_l = k_s$	16 W/(m °C)
$L$	$325 \times 10^3 \text{ J/kg}$

Table 2: Thermo-physical properties for Titanium

### 3. Modelling Selective Laser Melting

Goal of this section is to present a method that discretizes dynamically growing structures and in which refinements are only carried out where necessary. To this end, we first introduce the finite cell method, an embedded domain method for high-order finite elements, before moving on to a show-case example demonstrating the features of this approach.

#### 3.1. Finite Cell Method

The main objective of the finite cell method is to avoid boundary conforming meshing of geometrically complex physical domains. To this end, a geometrically complex domain  $\Omega_{phy}$  is extended by a fictitious domain  $\Omega_{fict}$  such that the resulting domain  $\Omega$  has a simple shape and can thus be meshed easily. (see fig. 10) and [26, 27].

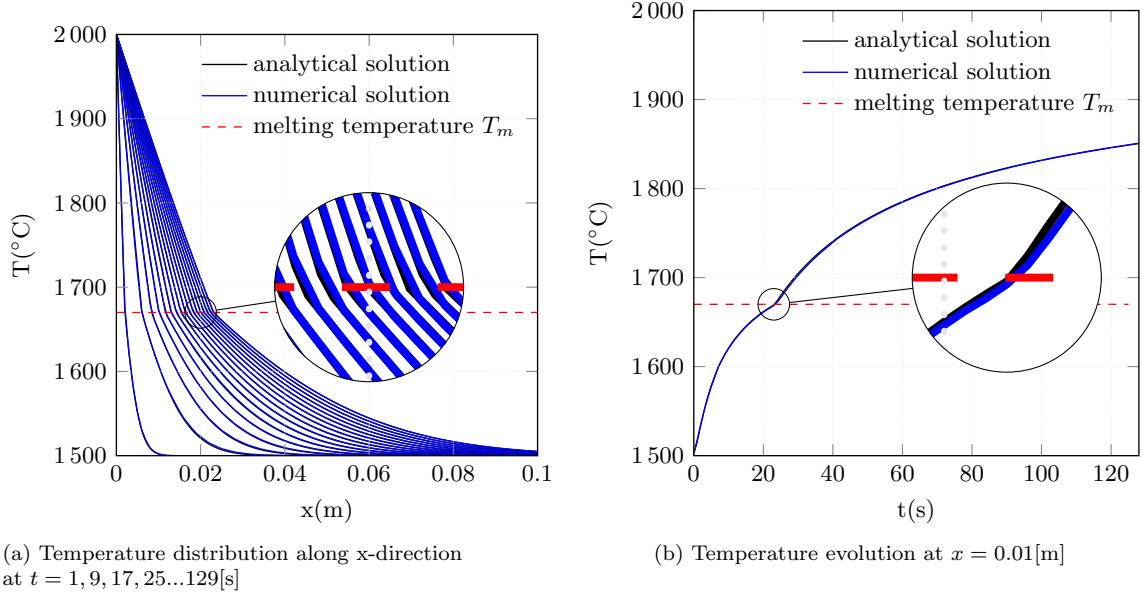


Figure 9: Melting bar example: evolution of temperature in time and space

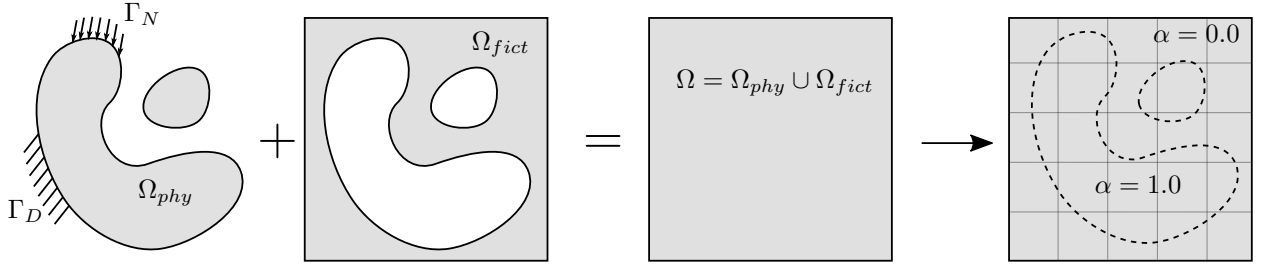


Figure 10: Concept of Finite Cell Method

In the simplest case, the mesh is a grid whose entities are called cells, henceforth the name finite cell method. It is on these cells where the shape functions are spanned. The original geometry of the domain is recovered at integration level by use of the following indicator function

$$\alpha = \begin{cases} 1 & \forall \mathbf{x} \in \Omega_{phy} \\ 10^{-g} & \forall \mathbf{x} \in \Omega_{fict} \end{cases} \quad (30)$$

where, ideally  $g \rightarrow \infty$ , although in practical applications it is usually sufficient to choose  $g = 4$ . The equality of a conforming to a non-conforming Galerkin formulation can easily be shown. For example for

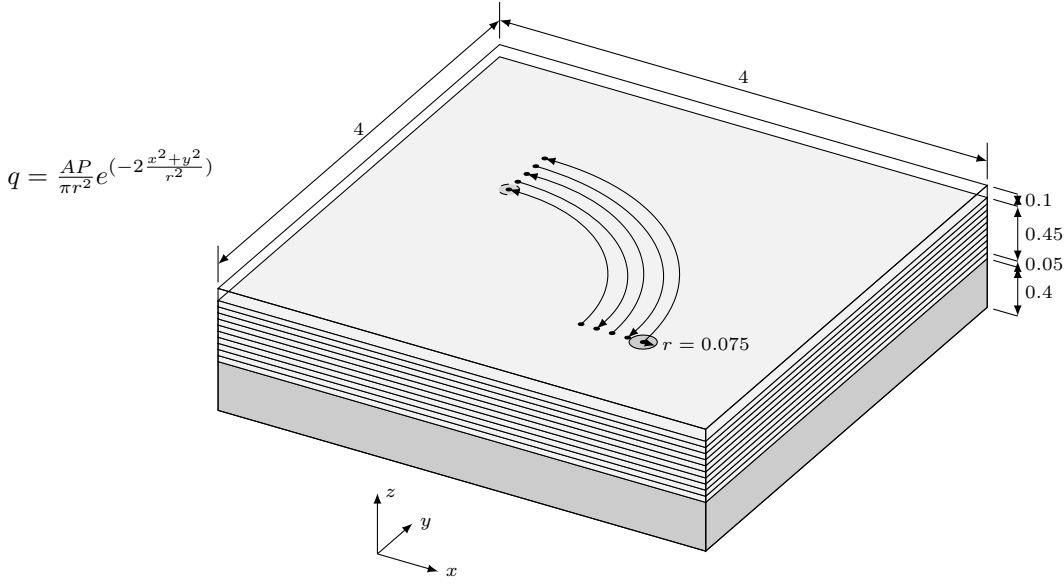


Figure 11: Setup of the process model

the volumetric term of  $K_{ij}$  given in eq. (14) it holds:

$$\begin{aligned}
 K_{ij} &= \int_{\Omega_{phy}} \nabla N_i \cdot (k \nabla N_j) d\Omega_{phy} \\
 &\approx \int_{\Omega_{phy}} \nabla N_i \cdot (1 k \nabla N_j) d\Omega_{phy} + \int_{\Omega_{fict}} \nabla N_i \cdot (10^{-g} k \nabla N_j) d\Omega_{fict} \\
 &= \int_{\Omega} \nabla N_i \cdot (\alpha k \nabla N_j) d\Omega.
 \end{aligned} \tag{31}$$

All other terms involving volume integrals in eq. (14) can be treated likewise. The convergence of this scheme is mathematically proven in [28] where it is additionally shown that the influence of a non-zero  $\alpha$  is proportional to a (controllable) modeling error.

The discontinuity of  $\alpha$  necessitates adaptive integration schemes, see e.g. [29, 30] for a recent overview of possible schemes. The simplest (although not most efficient) choice is a composed integration by means of an octree. This variant will be used to compute the examples in this section.

### 3.2. Multi-level hp method and the finite cell method at work

We now consider the computational modeling of a SLM process as depicted in fig. 11. The computational domain consists of a solid base plate upon which one powder layer resides. A laser then solidifies the powder along the path specified in the illustration. A new layer of powder is added and the process repeats until 10 layers are completed. Each layer has a thickness of  $50[\mu\text{m}]$ . The three phases powder, solid and melt are assigned the temperature dependent material coefficients given in fig. 12. The dependency of the heat capacity is assumed to be the same for all three phases, while the conductivity is assigned individually to each phase. The initial temperature of deposited material and base plate is  $T = 200^\circ\text{C}$ . Radiation and convection boundary conditions were applied at the top surface using an emissivity of  $\epsilon = 0.8$  and a convection coefficient of  $h_{conv} = 5.7 [\text{W}/\text{m}^2\text{C}]$ . Homogeneous Neumann boundary conditions are applied elsewhere.

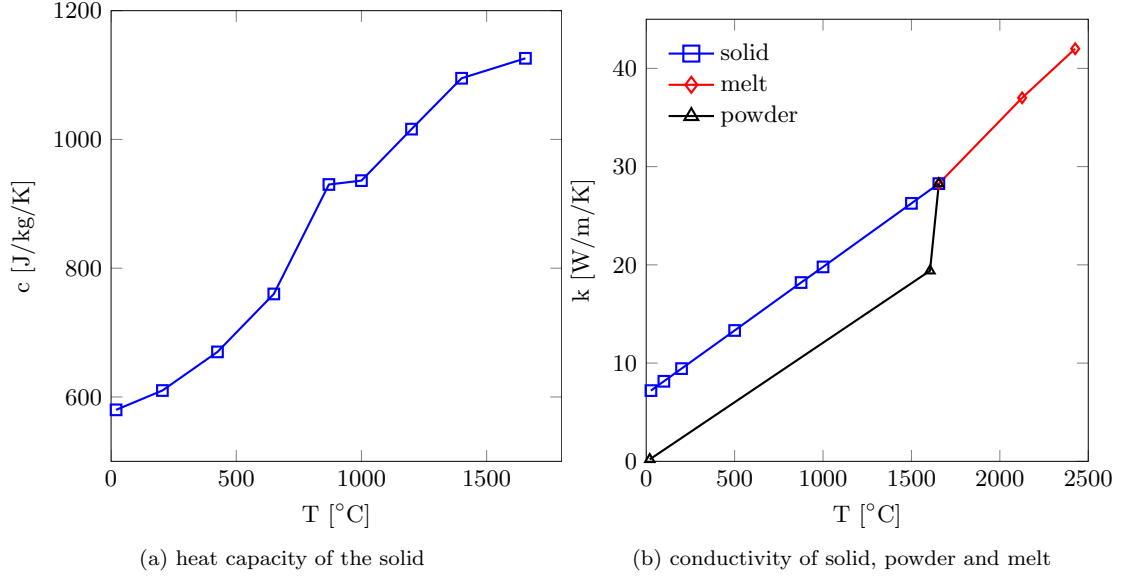


Figure 12: Temperature dependent material properties

The discretizational treatment of the process itself is best explained by considering a time-step of the simulation process. Two grids are used. The grid depicted in fig. 13a describes the material in a voxel-like fashion, while the other grid depicted in fig. 13b spans the high-order shape functions used for finite cell discretization of the temperature.

On the material side, four types of domains are to be distinguished: air, powder, solid/liquid and the base-plate. The distinction between air and powder is modeled by using the  $\alpha$  defined by the finite-cell method (see 30). This interface is explicitly defined as a geometric input. The change between powder and melt, however, emerges as a result of the power input by the laser beam. This locally emerging change in material properties is modeled similar to the bar example presented in section 2.4.2. The difference is that once powder has changed to melt it cannot change back to powder; it can only vary between melt and solid thereafter.

The grid which spans the basis functions discretizing the temperature field depicted in Figure 13b initially consists of  $8 \times 8 \times 5$  base finite cells. It is refined by recursively bisecting the elements three times towards a (moving) bounding box in the close proximity of the impact point of the laser using the multi-level  $hp$ -method discussed in 2.3. The smallest elements have an element size of half of the layer thickness in  $z$ -direction and  $62.5[\mu\text{m}]$  in in-plane direction. This corresponds to  $2.4^2$  finite elements of order  $p = 3$  at the impact point of the laser which. Under the assumption that the accuracy scales with the number of elements within the impact point of the laser and the chosen polynomial degree as studied in section 2.4.1, it is possible to obtain a rough estimate on the accuracy of the computation. In that case the same resolution is obtained for five multi-level refinements which led to an accuracy of approx. 4[%] at  $p = 3$  (see fig. 7a black line with pentagon symbols). This is considered to be in the range of other modeling errors which are even more difficult to track but naturally occur in the modeling of powder bed fusion processes.

The base level of the grid describing the material coefficients is geometrically and topologically congruent to the one used for the temperature discretization but both grids refine and de-refine independently of one another. The maximum refinement of the grid discretizing the state variables is one level finer than the thermal counterpart. It refines towards sudden changes in the material coefficients. This grid is used for a partitioned integration of the bilinear forms. The emerging structure (logged in that grid) is depicted along with the temperature in all physical domains at the representative time steps 220, 1000 and 1670 in figs. 14a to 14c, respectively.

At this point it is interesting to note the difference to other approaches common in the modelling



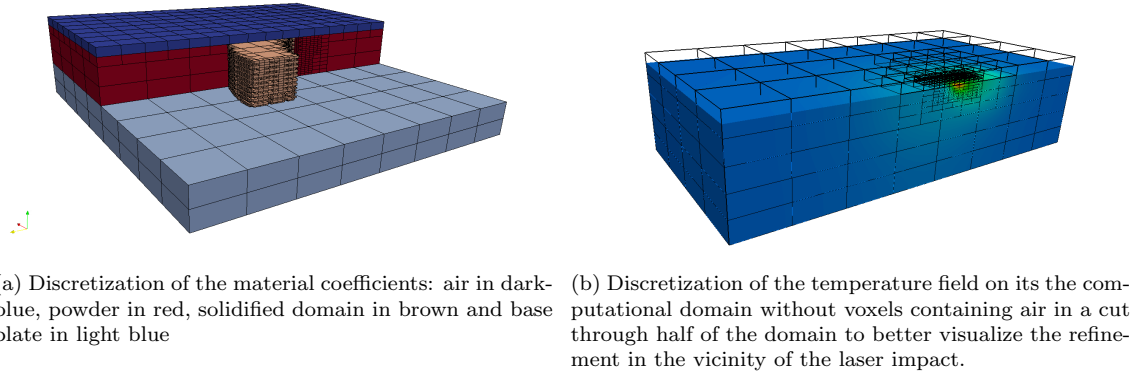


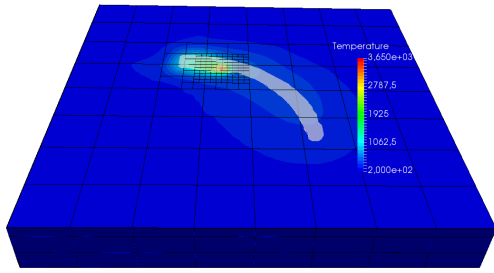
Figure 13: Discretization of material and temperature by means of two grids

of powder bed fusion processes or metal deposition: the quiet element method and the inactive element method. A comprehensive overview of both strategies is found e.g. in [31, 32, 33] including a discussion of each methods' advantages and disadvantages. In essence, the inactive element method activates elements in the sense of including them in the global stiffness matrix only if material was deposited in the region covered by the element. In the quiet element method, finite elements are active throughout all time steps of the simulation but are assigned small conductivities and capacities if no material is present. In this sense, the presented methodology is more related to the quiet element method because regions with no material are assigned low material properties. The difference lies in the fact that by using the finite cell method sub-regions within finite cells contain material while other regions of the cell may still be void. In the presented example, in the region of maximum refinement each layer consists of four layers of voxels. In turn, four layers are themselves contained in one finite cell at base level. One finite cell, thus, contains up to 16 voxels in  $z$ -direction. These voxels don't contribute to the number of degrees of freedom to be solved for. Nevertheless, they increase the resolution of the material properties provided that high-order shape functions are used to discretize the cells. As a consequence, a comparatively low number of degrees of freedom suffices for an accurate description of the field variables, e.g. the transient temperatures on evolving domains. The large gradients in the solution are captured accurately by using the multi-level  $hp$ -method and the necessary refinements can be kept local to the impact region of the laser beam. Figure 14d depicts the number of degrees of freedom for each time step. It varies between six- and eight thousand and increases only marginally throughout the process. The periodic spikes occur at time steps where the laser jumps from one scan path to another while the large plateaus show the change from one layer to another. The complete computation took approximately 10 hours for 2000 time steps on a standard desktop computer whereby only 45 minutes cpu time were actually used for solving the resulting non-linear equation system. This clearly indicates that there is room for optimizations.

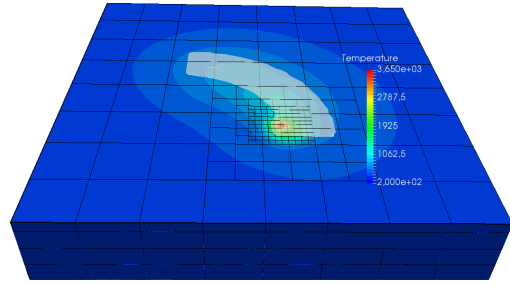
#### 4. Conclusions

The article at hand presents a computational framework for the simulation of powder bed fusion processes. The scheme is motivated by the fact that the very strong temperature gradients introduced locally by the laser beam quickly diffuse away while the state of the material does not diffuse. Therefore, the discretization of the temperature field is separated from the discretization of the material. These two separate meshes can then refine and coarsen independently of each other. The computational methodology is verified against two (semi-)analytical benchmarks. It is demonstrated that the combination of local refinements and high polynomial degree of the discretizations leads to higher accuracies than only decreasing the mesh size.

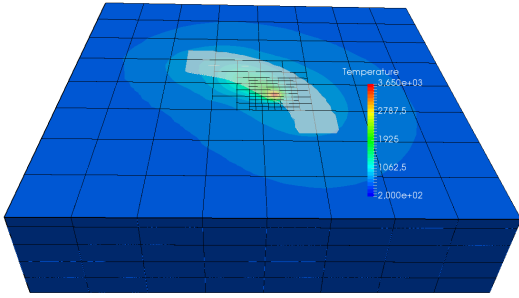
The closing example serves to demonstrate the discretizational flexibility of the method for the simulation of the temperature evolution and the phase changes involved in SLM processes. Herein, the material layers do not conform to the discretization of the temperature field and the number of the degrees of freedom are



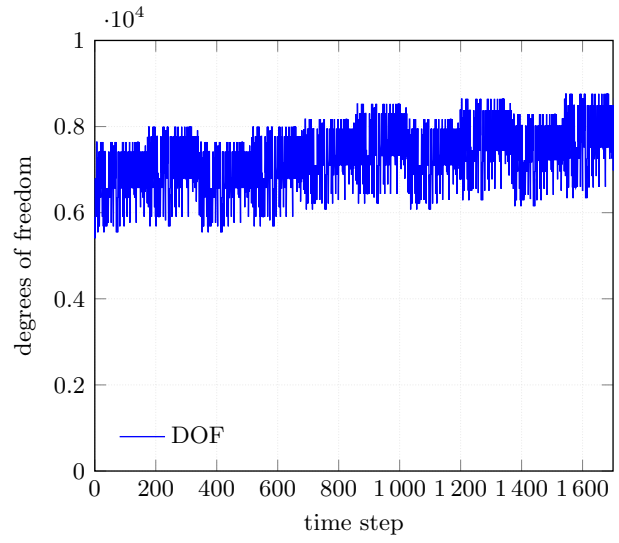
(a) time step 220



(b) time step 1000



(c) time step 1670



(d) DOF over time

Figure 14: Temperature field and its discretization with emerging structure at different time steps and number of degrees of freedom for all time steps throughout the process

decoupled from the length of the laser scan path. This flexibility in the discretization allows for a practically constant number of degrees of freedom throughout the entire the computation.

Future research will be directed into extending the methodology to include multi-physical capabilities such as the computation of thermo-elasto-plastic phenomena in multi-layer processes.

## Acknowledgements

The authors gratefully acknowledge the financial support of the German Research Foundation (DFG) under Grant RA 624/27-1.

- [1] W. D. Rolph and K.-J. Bathe, "An efficient algorithm for analysis of nonlinear heat transfer with phase changes," *International Journal for Numerical Methods in Engineering*, vol. 18, no. 1, pp. 119–134, 1982.
- [2] I. Babuška and B. Q. Guo, "The h, p and h-p version of the finite element method; basis theory and applications," *Advances in Engineering Software*, vol. 15, no. 3, pp. 159–174, 1992.
- [3] L. Demkowicz, *Computing with Hp-Adaptive Finite Elements, Vol. 1: One and Two Dimensional Elliptic and Maxwell Problems*. Applied mathematics and nonlinear science series, Boca Raton: Chapman & Hall/CRC, 2007.
- [4] D. Riedlbauer, P. Steinmann, and J. Mergheim, "Thermomechanical finite element simulations of selective electron beam melting processes: Performance considerations," *Computational Mechanics*, vol. 54, pp. 109–122, July 2014.
- [5] J. Irwin and P. Michaleris, "A line heat input model for additive manufacturing," *Journal of Manufacturing Science and Engineering*, vol. 138, no. 11, 2016.
- [6] Q. Wang, J. Li, M. Gouge, A. R. Nassar, P. P. Michaleris, and E. W. Reutzel, "Physics-Based Multivariable Modeling and Feedback Linearization Control of Melt-Pool Geometry and Temperature in Directed Energy Deposition," *Journal of Manufacturing Science and Engineering*, vol. 139, no. 2, p. 021013, 2017.
- [7] W. Rachowicz and L. Demkowicz, "An hp-adaptive finite element method for electromagnetics: Part 1: Data structure and constrained approximation," *Computer Methods in Applied Mechanics and Engineering*, vol. 187, pp. 307–335, June 2000.
- [8] W. Rachowicz, D. Pardo, and L. Demkowicz, "Fully automatic hp-adaptivity in three dimensions," *Computer Methods in Applied Mechanics and Engineering*, vol. 195, pp. 4816–4842, July 2006.
- [9] Hermes, "Hermes - Higher-Order Modular Finite Element System," user's guide, University of Reno, Nevada, USA, 2016.
- [10] P. Šolín and J. Červený, "Automatic hp-Adaptivity with Arbitrary-Level Hanging Nodes," Tech. Rep. Research Report No. 2006-07, The University of Texas at El Paso, Department of Mathematical Sciences, 2006.
- [11] N. Zander, T. Bog, M. Elhaddad, F. Frischmann, S. Kollmannsberger, and E. Rank, "The multi-level hp-method for three-dimensional problems: Dynamically changing high-order mesh refinement with arbitrary hanging nodes," *Computer Methods in Applied Mechanics and Engineering*, vol. 310, pp. 252–277, Oct. 2016.
- [12] D. Celentano, E. Oñate, and S. Oller, "A temperature-based formulation for finite element analysis of generalized phase-change problems," *International Journal for Numerical Methods in Engineering*, vol. 37, no. 20, pp. 3441–3465, 1994.
- [13] W. Bangerth, R. Hartmann, and G. Kanschat, "deal.II—A general-purpose object-oriented finite element library," *ACM Transactions on Mathematical Software*, vol. 33, pp. 1–27, Aug. 2007. 00582.
- [14] "Nektar++, A Spectral/hp Element Framework."
- [15] W. F. Mitchell, "PHAML." <http://math.nist.gov/phaml/phaml.html>.
- [16] P. Karban, F. Mach, P. Kús, D. Pánek, and I. Doležal, "Numerical solution of coupled problems using code Agros2D," *Computing*, vol. 95, pp. 381–408, May 2013. bibtex karban\_numerical:2013.
- [17] L. Dalcin, N. Collier, P. Vignal, A. M. A. Côrtes, and V. M. Calo, "PetIGA: A framework for high-performance isogeometric analysis," *Computer Methods in Applied Mechanics and Engineering*, 2016.
- [18] N. Zander, T. Bog, S. Kollmannsberger, D. Schillinger, and E. Rank, "Multi-level hp-adaptivity: High-order mesh adaptivity without the difficulties of constraining hanging nodes," *Computational Mechanics*, vol. 55, pp. 499–517, Feb. 2015.
- [19] N. Zander, M. Ruess, T. Bog, S. Kollmannsberger, and E. Rank, "Multi-level hp-adaptivity for cohesive fracture modeling," *International Journal for Numerical Methods in Engineering*, vol. in press, 2016.
- [20] P. Di Stolfo, A. Schröder, N. Zander, and S. Kollmannsberger, "An easy treatment of hanging nodes in hp-finite elements," *Finite Elements in Analysis and Design*, vol. 121, pp. 101–117, Nov. 2016.
- [21] N. T. Nguyen, A. Ohta, K. Matsuoaka, N. Suzuki, and Y. Maeda, "Analytical solutions for transient temperature of semi-infinite body subjected to 3-D moving heat sources," *WELDING JOURNAL-NEW YORK-*, vol. 78, pp. 265–s, 1999. 00148.
- [22] L. Shampine, "Vectorized adaptive quadrature in MATLAB," *Journal of Computational and Applied Mathematics*, vol. 211, pp. 131–140, Feb. 2008.
- [23] H. Weber, "Die Partiellen Differentialgleichungen der Mathematischen Physik." <https://ia601408.us.archive.org/4/items/diepartiellendi00riemgoog/diepartiellendi00riemgoog.pdf>, 1912.
- [24] H. Hu and S. A. Argyropoulos, "Mathematical modelling of solidification and melting: A review," *Modelling and Simulation in Materials Science and Engineering*, vol. 4, no. 4, p. 371, 1996.
- [25] D. W. Hahn, *Heat Conduction*. Hoboken, N.J: Wiley, 3rd ed ed., 2012.
- [26] J. Parvizian, A. Düster, and E. Rank, "Finite cell method," *Computational Mechanics*, vol. 41, pp. 121–133, Apr. 2007.
- [27] A. Düster, J. Parvizian, Z. Yang, and E. Rank, "The finite cell method for three-dimensional problems of solid mechanics," *Computer Methods in Applied Mechanics and Engineering*, vol. 197, pp. 3768–3782, Aug. 2008.

- [28] M. Dauge, A. Düster, and E. Rank, “Theoretical and Numerical Investigation of the Finite Cell Method,” Journal of Scientific Computing, vol. 65, pp. 1039–1064, Mar. 2015. 00000.
- [29] A. Abedian, J. Parvizian, A. Düster, H. Khademyzadeh, and E. Rank, “Performance of Different Integration Schemes in Facing Discontinuities in the Finite Cell Method,” International Journal of Computational Methods, vol. 10, p. 1350002, June 2013. 00027.
- [30] L. Kudela, N. Zander, S. Kollmannsberger, and E. Rank, “Smart octrees: Accurately integrating discontinuous functions in 3D,” Computer Methods in Applied Mechanics and Engineering, vol. 306, pp. 406–426, July 2016.
- [31] P. Michaleris, “Modeling metal deposition in heat transfer analyses of additive manufacturing processes,” Finite Elements in Analysis and Design, vol. 86, pp. 51–60, Sept. 2014. 00006.
- [32] M. Chiumenti, M. Cervera, A. Salmi, C. Agelet de Saracibar, N. Dialami, and K. Matsui, “Finite element modeling of multi-pass welding and shaped metal deposition processes,” Computer Methods in Applied Mechanics and Engineering, vol. 199, pp. 2343–2359, Aug. 2010.
- [33] L.-E. Lindgren and E. Hedblom, “Modelling of addition of filler material in large deformation analysis of multipass welding,” Communications in numerical methods in engineering, vol. 17, no. 9, pp. 647–657, 2001.